Corrosion of 316H Stainless Steel in Flowing FLiNaK Salt

Stephen S. Raiman[a], J. Matthew Kurley[b], Dino Sulejmanovic[c], Adam Willoughby[c], Scott Nelson[b], Keyou Mao[c], Chad Parish[c], M. Scott Greenwood[b], Bruce A. Pint[c]

a. Department of Nuclear Engineering, Texas A&M University
b. Nuclear Energy and Fuel Cycle Division, Oak Ridge National Laboratory
c. Materials Science and Technology Division, Oak Ridge National Laboratory

Abstract

Type 316H stainless steel samples were exposed to flowing FLiNaK salt for 1000h in a thermal convection loop with a maximum temperature of 650°C and a minimum of 540°C. Samples in the hottest part of the loop lost mass, with a maximum mass loss of 1.8 mg/cm^2, while samples in the coldest parts of the loop gained mass. Analysis of the samples that gained mass showed an iron-rich layer on the sample surfaces, suggesting that iron, not chromium, accounted for the majority of the mass transfer in the loop. Analysis of the salt showed major increases in the Cr, Fe, and Mn content of the salt during exposure. The loop was modeled using the TRANSFORM code. Modeled values matched the experimental temperature measurements showing that TRANSFORM is capable of accurately simulating the conditions in the loop.

Introduction

Molten salt reactors (MSR) are a Generation IV reactor technology that has gained increasing attention in recent years[1,2]. While the use of molten salts as coolant and/or fuel media offers many advantages, compatibility with structural materials must be ensured before deployment of an MSR. Materials testing for molten salt compatibility dates back to the Aircraft Nuclear Propulsion (ANP) program at Oak Ridge National Laboratory (ORNL) in the 1950s [3], and continued throughout the Molten Salt Reactor Experiment (MSRE) and Molten Salt Breeder Reactor (MSBR) programs in the 1960s and 1970s[4–9].

The Oak Ridge experimenters made extensive use of flowing experiments to test alloy compatibility with molten salts. While a static test is easier and less expensive, the eventual saturation of the static salts with corrosion product limits the usefulness of static testing for predicting corrosion rates. By circulating salt through a loop that imposes a change in temperature as salt traverses the circuit, corrosion associated with mass transfer can be driven indefinitely without saturating the salt with corrosion products. The driving force for corrosion over long time scales in a flowing system is the collection of temperature-dependent equilibria that result in the depletion of alloy components in the hottest parts of the loop, and the deposition of corrosion products in the cold parts of the loop[3,6,10,11]. Loops with a temperature

differential mimic the conditions in an MSR in which salt would be hottest in the reactor core, and colder in the heat exchanger.

Thermal convection loops (TCLs) have been used since the ANP program to test material-salt combinations[3]. Central to the design are a pair of vertical tube lengths, one heated and one not heated. The difference in salt density between the two vertical sections creates a natural convective flow that circulates the salt in the loop without the expense and complexity of a pump or valves. TCLs were used extensively during the ARE and MSRE eras at ORNL[4,6,8,12], and in later years for studying compatibility with salt and liquid metal for fusion energy[13–15]. With the recent surge in interest in MSRs, TCLs have been operated at the Kurchatov Institute[16] and The University of Wisconsin[17] and ORNL[18,19]

A great deal of early work on material compatibility with fluoride salts was focused on Ni-based alloys. Alloy N, developed at ORNL specifically for use as a fluoride salt-facing structural material[20,21], was used extensively in the MSRE[22]. Recent attention has turned to evaluating the compatibility of molten salts with stainless steels[23–26]. Stainless steels were the subject of some study during the MSRE era as well[5,8,27]. Type 316H is the high-carbon version of type 316 stainless steel (SS), and is ASME code qualified for higher-temperature service. It is attractive because it is available in common forms, and is generally less expensive than nickel-based superalloys.

The purpose of this work is to evaluate corrosion and mass transfer of type 316H SS in flowing fluoride salt. Coupons were exposed to flowing FLiNaK salt with a maximum temperature of 650°C in a TCL. The samples were characterized to understand the extent and nature of mass transfer and compared to similar specimens exposed in static experiments. A TRANSFORM model was created to understand the heat flow in the loop.

Experiment

Loop Construction

Exposures were conducted in a redesigned TCL. A photograph, 2D drawing and a 3-D rendering of the loop are shown in Figure 1. The loop was constructed from ¾" schedule 40 pipe, with an outer diameter of 26.7mm, an inner diameter of 20.8mm, and a wall thickness of 2.79mm. All dimensions are nominal, and based on ASTM A53[28]. An overflow tank was positioned at the top of the hot leg, and a SS fill tank was connected above that. Three 900 W heaters were positioned on the loop, two on the hot leg and one on the bottom leg. The whole loop was wrapped in heating tape to allow for greater control over temperature. Thermocouples were positioned in thermowells around the loop, as indicated on the 2D drawing.

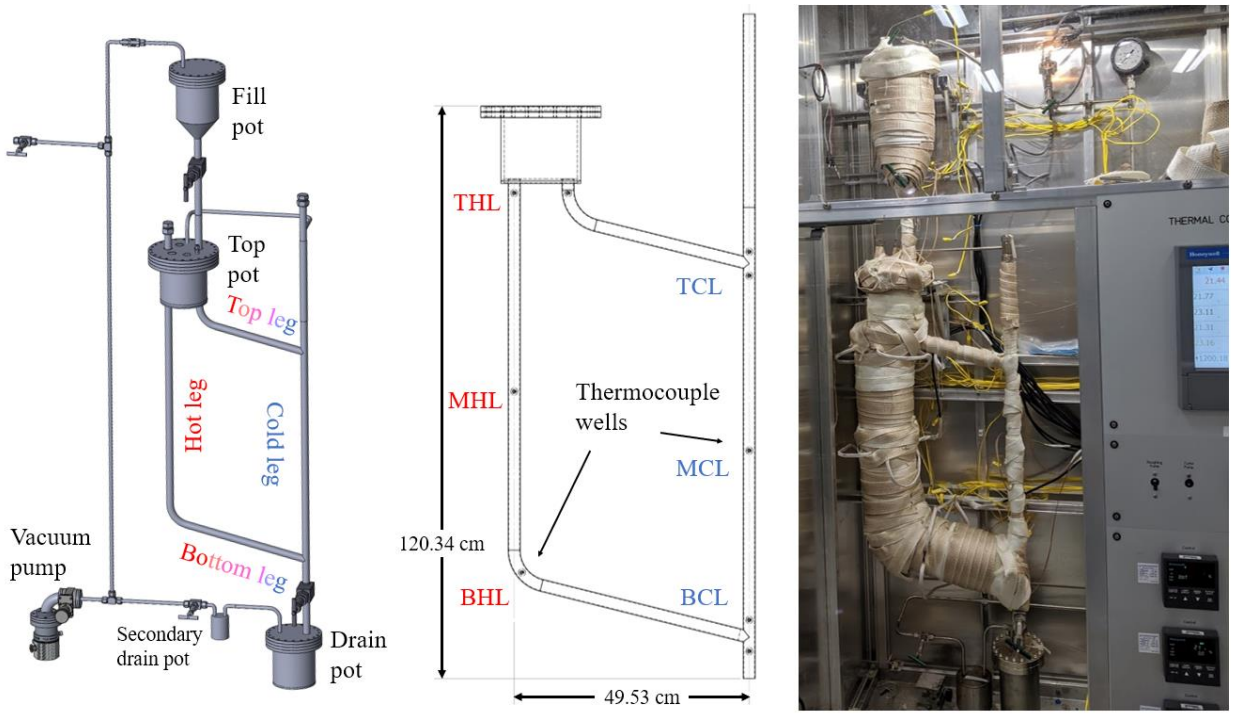

Figure 1. The thermal convection loop used for this study. (a)A 3D rendering, (b) 2D drawing, and (c)a photograph of the loop with heaters and insulation. In (b), thermowells are shown at the top (T), middle (M) and bottom (B) of the hot leg (HL) and cold leg (CL).

Salt preparation

The FLiNaK salt used for this work was prepared by Electrochemical Systems, a now defunct company that specialized in salt purification for research projects. It was recovered from old-stock, stored in airtight Ni alloy vessels. Salts were handled only in inert gloveboxes, so moisture did not come in contact with the salts at any stage. Due to the age of the salt, details of its provenance are unknown, although hydrofluorination is believed to have been the primary method of impurity removal[29]. The as-received salt was analyzed with inductively coupled plasma mass spectroscopy (ICP-MS) by the University of Wisconsin Hygiene Lab, and the results are shown in Table 1. Due to the lack of a reliable method for measuring moisture content, only metallic impurities are reported. Previous reports of similar FLiNaK salts from the same source suggested it was relatively pure with low corrosivity[30].

Table 1. Salt contents before exposure, as measured by ICP-MS. All values in µg/g.

K	**Na**	**Li**	**Zr**	**Ba**	**Ca**	**Ti**	**Mg**
385427.3	75409.95	74920	366.31	147.49	75.013	56.17	20.93
Rb	**Al**	**Fe**	**Ni**	**Cr**	**S**	**Sr**	**Hf**
17.23	12.46	7.17	6.66	4.57	4.56	2.06	0.99
Mn	**Se**	**B**	**Sc**	**Ag**	**Be**	**P**	**Mo**
0.88	0.70	0.53	0.39	0.37	0.26	0.22	0.16

Sample preparation

Samples were cut from 316H plate. The composition of the heat is given in Table 2. Composition was measured using ICP-MS and optical emission spectroscopy, inert gas fusion, and combustion analysis. Two types of samples were prepared. 12 coupons measuring 25.4 x 19 x 2 mm and 28 SS-3 tensile specimens. The specimens were arranged in chains, held together by alloy 600 wire, and are shown in Figure 2. Spacers were positioned at the top and middle of each chain to ensure they remained centered within the vertical tubing of the TCL.

Table 2. Composition of the heat of type 316H SS used to make samples for this work, determined by ICP-MS and combustion analyses.

	Fe	Ni	Cr	Mo	Mn	Si	C	S	O	others
316H	64.5	13.3	17.2	2.3	1.9	0.54	0.058	0.016	0.008	Cu 0.08

Figure 2. 316H sample chains that were hung in the vertical portions of the loop, one in the hot leg, and one in the cold leg.

Capsule testing

As a preliminary step, 316H samples measuring 12.7 x 6.4 mm were statically exposed to the same FLiNaK salt in 316H or low carbon arc cast molybdenum capsules. Each cylindrical capsule measured 7.6 cm in length by 2.5 cm in diameter. Samples were tethered to one end of each capsule, and capsules were filled with 30g of solid FLiNaK salt. The capsules were welded shut in the same glovebox without exposure to air. The capsules were then sealed within outer SS capsules to provide secondary containment. A full description of the capsule testing procedure is available in Ref[31]. For this work, the capsules were welded in an argon-filled glovebox with a TIG welder, so argon was present with the FLiNaK in the capsules for the present work but there was no opportunity for air ingress when loading capsules into an e-beam welder. A total of 12 capsules were heated in a box furnace for 1000h at either 550 or 650°C. The sample matrix is shown in Table 3.

Table 3. Experimental conditions for static testing of 316H samples.

	550°C	650°C
316H capsule	3	3

Mo capsule	3	3

Loop Testing Procedure

Sample chains were hung from the top of the vertical portions of the loop with type 310 SS wire measuring ~16" long on the hot leg, and ~24" on the cold leg. This wire represents the only dissimilar metal in the loop, and its surface area was relatively very small and unlikely to affect corrosion of the other specimens. The top pot was filled with FLiNaK salt in an inert glovebox, sealed, and positioned on top of the loop. With the loop sealed, it was pumped down to a vacuum of ~$7x10^{-3}$ Pa, heated to ~200°C, and allowed to out-gas for ~2.5 days.

To begin the experiment, the loop including the top pot was heated above the melting point of FLiNaK (454°C). The valve below the fill pot was opened, and the salt was allowed to drain into the body of the loop, filling it to a depth approximately half way up the overflow pot. The heaters and heating tape were used to achieve a maximum target temperature of 650°C at the top of the hot leg, and 550°C at the bottom of the cold leg, which was sufficient to drive convective flow around the loop.

The loop was operated for 1000 h at steady state. At the conclusion of the 1000 h, the valve at the bottom of the cold leg was heated and then opened, allowing the salt to immediately flow into the drain tank, where it cooled to room temperature, along with the loop. The drain tank was removed from the loop and stored in a glovebox so the salt could be analyzed. The solid salt was briefly exposed to air (<10 minutes) during this transfer, but surface area was minimal due to the single solid form of the salt. The loop was filled with DI water and drained 3 times to remove residual salt from the samples, followed by a rinse with acetone before the sample chains were removed.

Analysis

Individual samples were cleaned by sonicating in ~50°C water for at least 1 h to remove any further traces of residual salt. Specimen mass change was measured with a Mettler Toledo model XP205 balance with an accuracy of ±0.04 mg. Samples were cross-sectioned, mounted in epoxy, polished, and imaged optically with a Leica model MEF4A microscope. Samples were also characterized with scanning electron microscopy (SEM) and energy dispersive spectroscopy (EDS) mapping on a Hitachi S-4800 equipped with EDAX hardware. Salts were analyzed by ICP-MS on a Thermo-Finnigan Element 2 instrument. Samples were digested using microwave digestion in 7.0 mL of 16 M nitric acid, 3.0 mL of 12 M hydrochloric acid, 2.0 mL of 28 M hydrofluoric acid and 3.0 mL of DI water. After digestion, samples were diluted using several different ratios to account for a wide range of concentrations of analytes.

Results

The samples exposed to static FLiNaK salt in capsules were cleaned and weighed to determine mass change, and the results are shown in Figure 3. The samples exposed in 316H capsules had

lower mass loss than samples exposed in Mo capsules and indicated that the salt was relatively hifh purity. In both cases, the samples exposed at 650°C lost more mass than the samples exposed at 550°C.

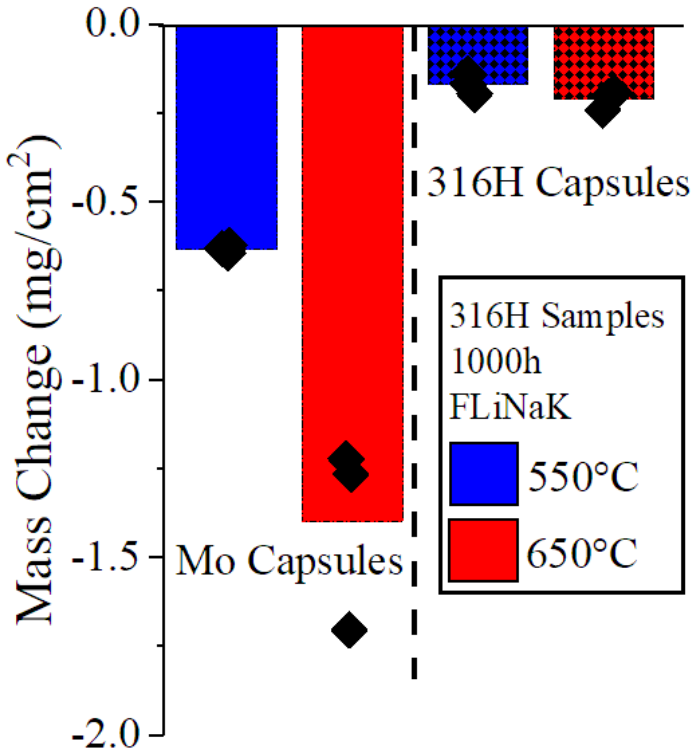

Figure 3. Mass change of 316H samples exposed to FLiNaK salt in 316H or Mo capsules for 1000h at 550 or 650°C.

The coupon samples exposed in the loop were also measured for mass change, and the results are shown in Figure 4 where the specimen mass change is plotted versus the exposure temperature. The temperature of each sample was not measured directly, but modeled in TRANSFORM (see discussion section). To determine the temperature of each sample, a linear rate of temperature change was assumed between the thermocouples in the hot and cold legs, and a temperature for each sample was assigned based on its position within the leg. The hottest samples were at the top of the hot leg, and the coldest samples were at the bottom of the cold leg.
All the samples in the hot leg lost mass, with a maximum mass loss of 1.8 mg/cm^2. Samples in the cold leg gained or lost mass, with a maximum gain of 1.1 mg/cm^2 and a maximum loss of 0.6 mg/cm^2. The mass change as a function of temperature appears roughly linear in Figure 4.

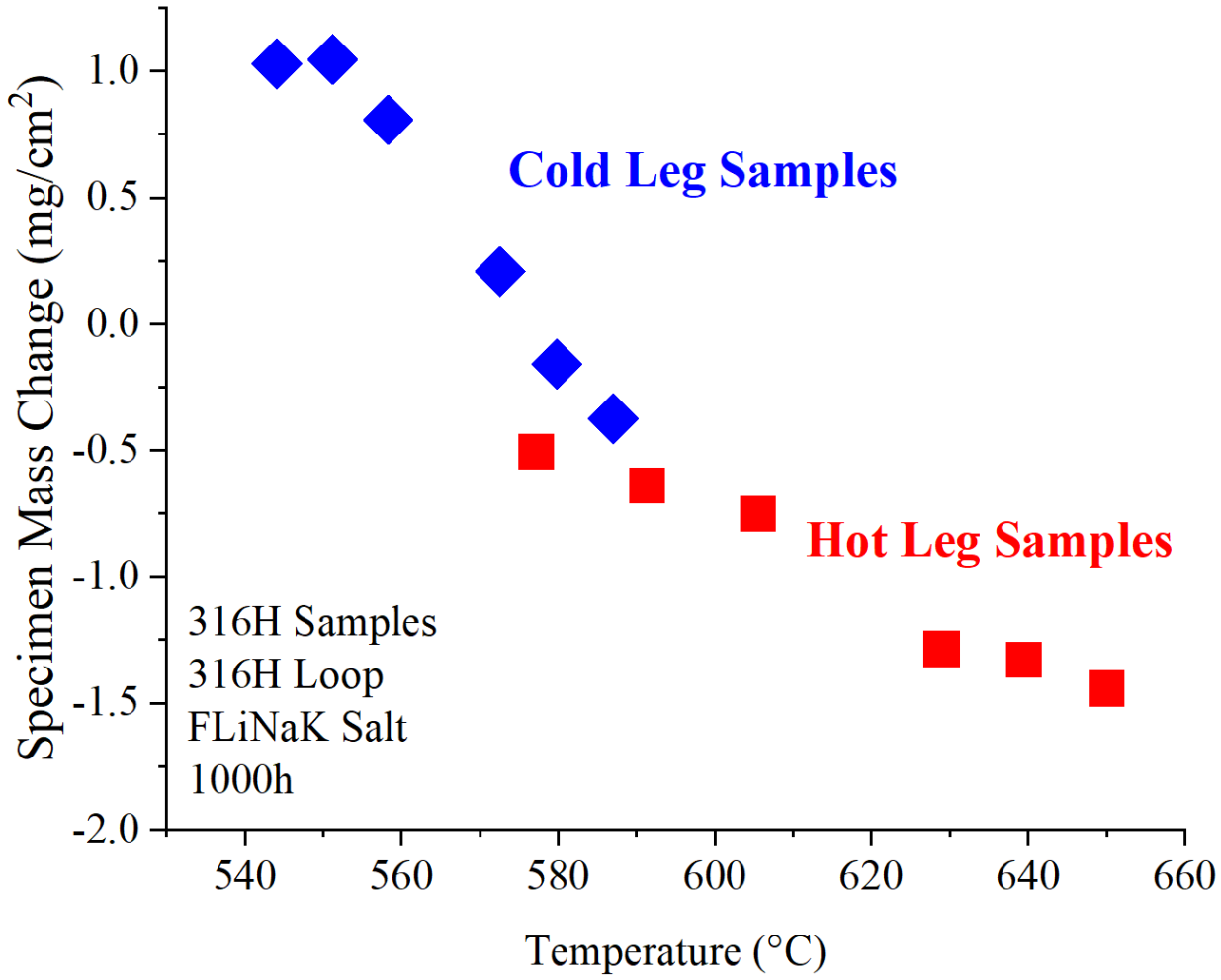

Figure 4. Mass change of 316H samples exposed to flowing FLiNaK salt for 1000h.

Light micrographs of the coupon polished cross-sections are shown in Figure 5. Subsurface attack is visible on hot leg samples H1-H6. A deposited layer is visible on samples C7-C12 and on H5-H6. Samples H5, H6, C7, and C8 all lost mass (Figure 4) suggesting that some of the original metal under the deposited layer must have been lost.

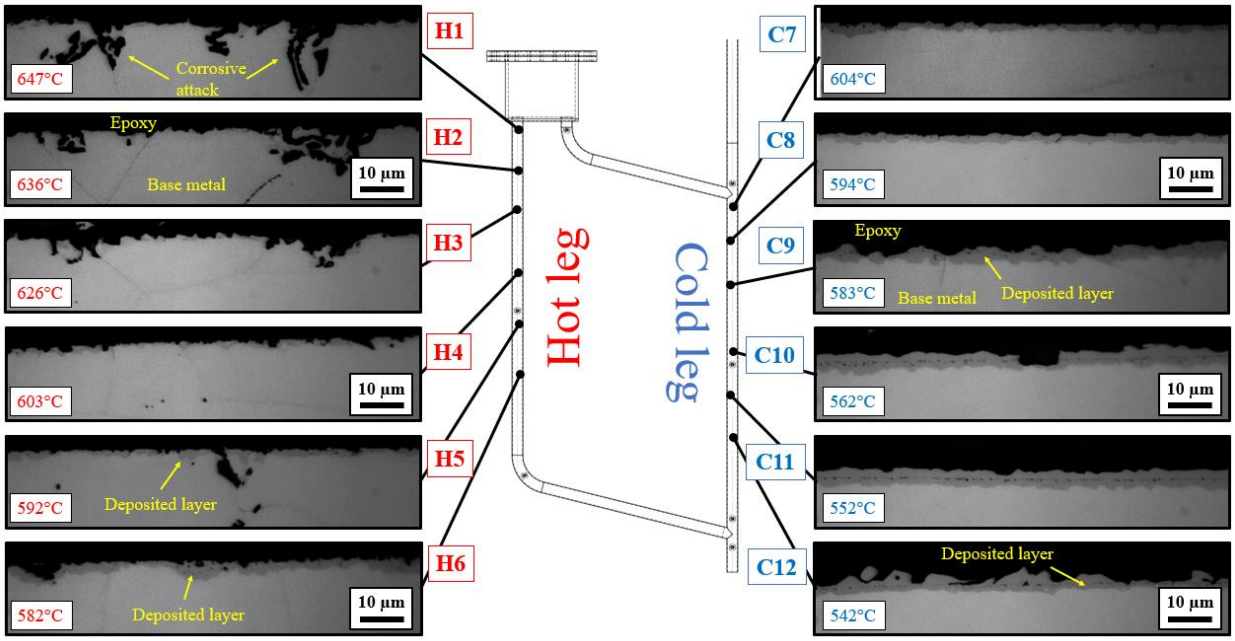

Figure 5. Light micrographs of 316H samples exposed for 1000h to flowing FLiNaK salt. Samples temperatures are from the TRANSFORM simulation, and sample locations are approximate

For each sample, depth of attack (for samples in the hot leg) or thickness of the deposited layer (for samples in the cold leg) was measured using image analysis and the results are shown in Figure 6. The hottest sample had an average depth of attack of approximately 5µm, while the coldest sample had a deposition layer with an average thickness of 3 µm.

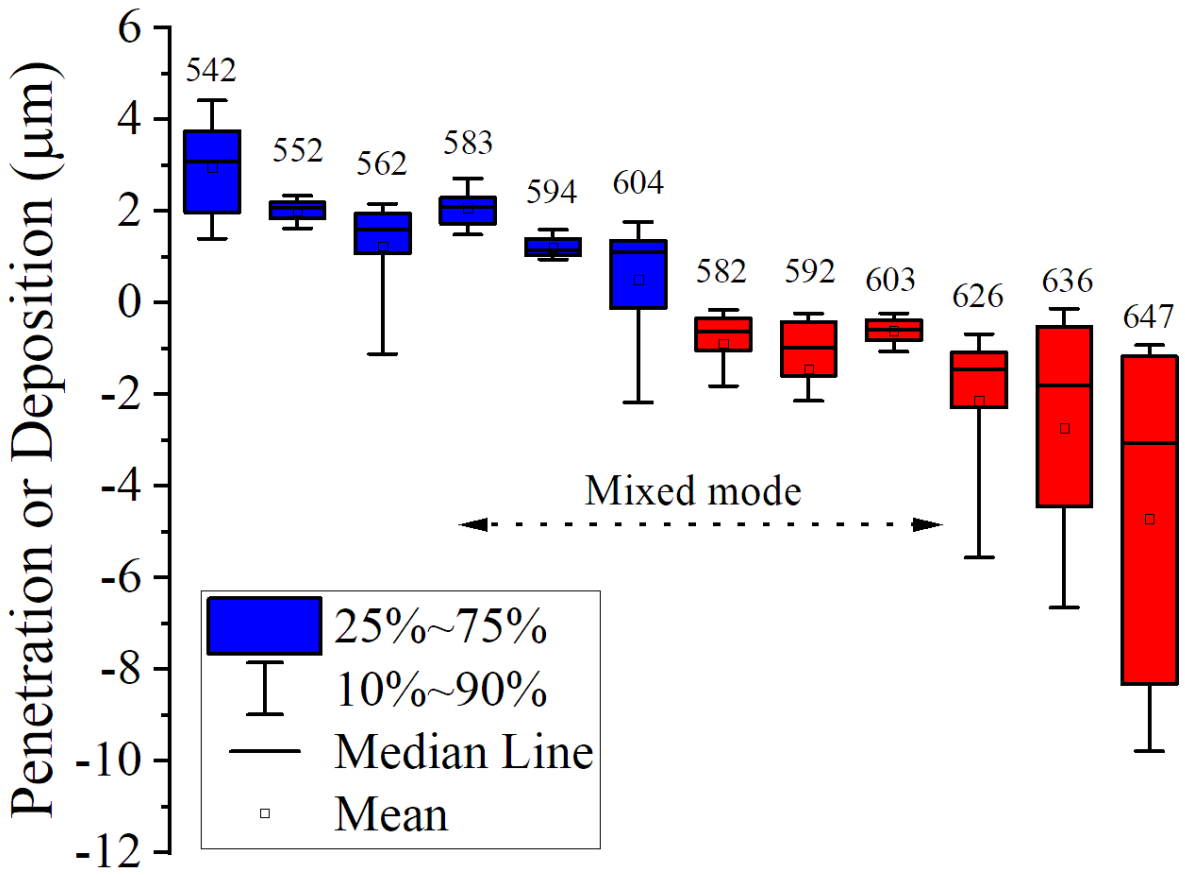

Figure 6. Depth of attack or thickness of the deposition layer for 316H samples exposed to flowing FLiNaK salt for 1000h. Calculated temperature of each sample in °C is displayed above each box.

EDS line scans were taken on each sample, and the results are shown in Figure 7. All of the cold leg samples have a deposit on the surface that is rich in Fe and low in Cr, and that is reflected in the line scans. Samples H5 and H6, the samples closest to the bottom of the hot leg, also have an Fe-rich deposit layer in addition to subsurface attack. The Ni content of the deposited layer in samples H5, H6, C7, and C8 is either the same as the bulk metal, or slightly higher. The line scans of samples C9-C12 show a deposited layer depleted in Ni. Line scans of the hot leg samples without a deposited layer, samples H1-H4, show Cr depletion near the surface. Iron is also depleted near the surface except on sample 3. Samples H1-H4 are also enriched in Ni near the surface.

SEM-EDS maps of samples H1 and C11 are shown in Figure 8. The attacked region on sample H1 is enriched in Ni, and depleted in Fe and Cr. Mo precipitates are visible in the attacked region. Sample C11 has a deposited layer rich in Fe, with little Ni, Cr, and Mn. Mo precipitates are also visible in the deposited layer.

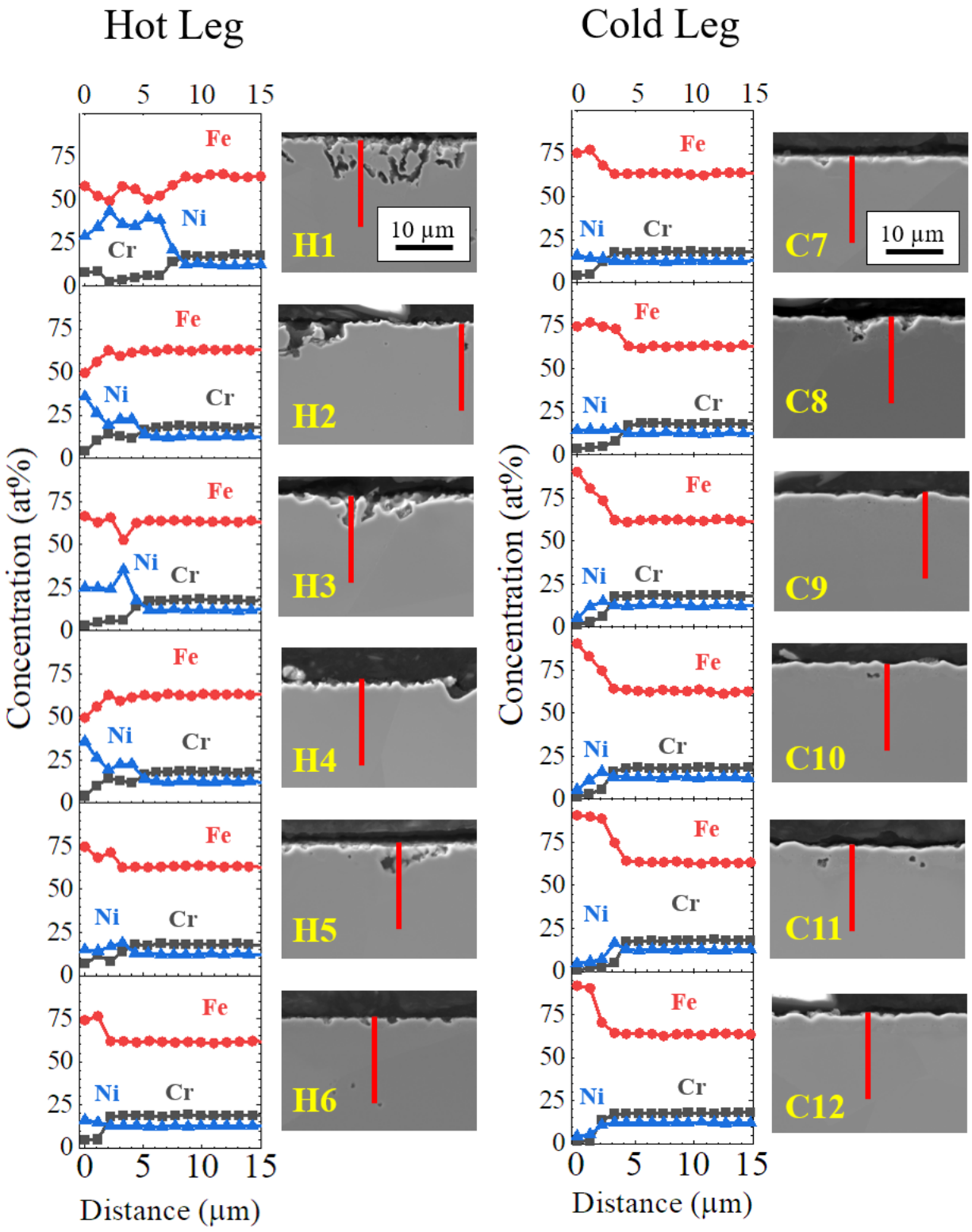

Figure 7. EDS scans of samples exposed to FLiNaK salt for 1000h at various locations in the loop

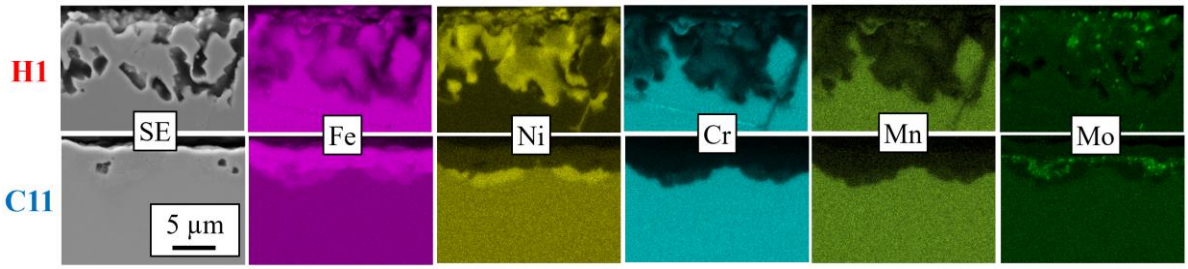

Figure 8. EDS map of 316H samples H1 and C11 exposed to flowing FLiNaK salt for 1000h at 647 and 552°C respectively

To further investigate the composition of the deposition layer, transmission electron microscopy (TEM) micrographs of samples H6 and C7 are shown in Figure 9. On H6, the metal is mostly Fe and Ni with Cr depleted from the matrix, but Cr and Mo-rich precipitates are visible throughout the matrix. Mo-rich precipitates are also visible near the surface and along what appears to be a grain boundary. On sample C7, the deposition layer is visible above the metal surface. The layer was Fe-rich oxide, although this may be due to air oxidation of the focused ion beam (FIB) lamella, as the Cr-depleted deposition layer would be susceptible to air oxidation. Cr and Mo precipitates are also visible in the metal matrix, and Mo-rich precipitates are visible in the deposition layer.

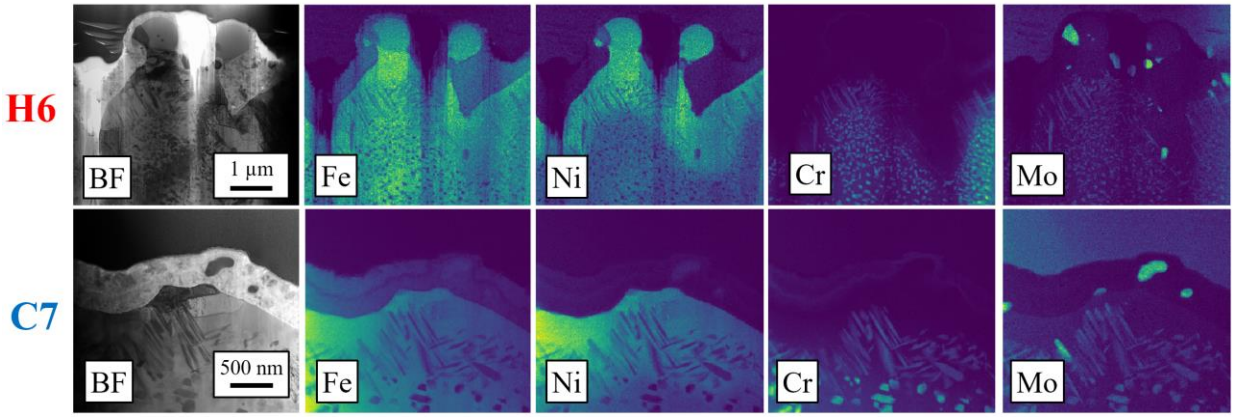

Figure 9. STEM-EDS map of 316H samples H6 and C7 exposed to flowing FLiNaK salt for 1000h at 582 and 604°C respectively

The concentration of metallic species in the salt was measured with ICP-OES before and after exposure, and the results are shown in Figure 10. The content of Fe, Cr, and Mn in the salt increased dramatically during exposure, while the Ni content decreased slightly.

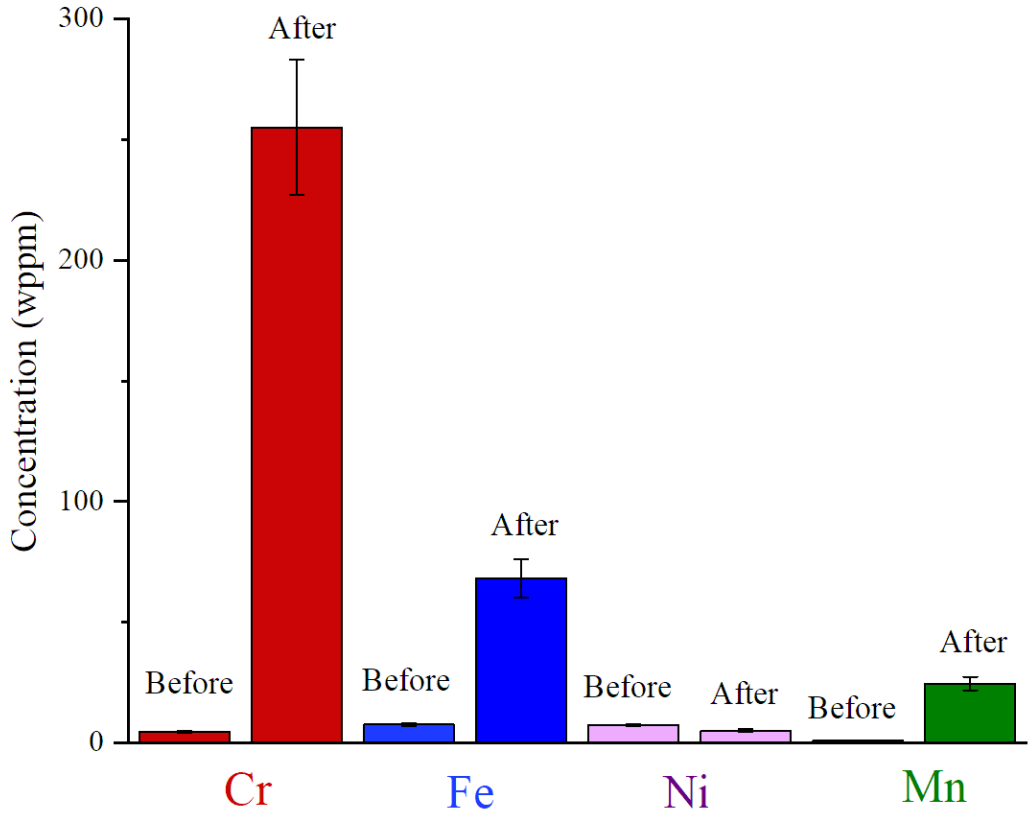

Figure 10. Concentration of metallic species in FLiNaK salt before and after flowing for 1000h in the 316H TCL.

TCL Temperature Model

A thermal-hydraulic system model was created utilizing the Transient Simulation Framework of Reconfigurable Models (TRANSFORM) code developed at Oak Ridge National Laboratory[32]. TRANSFORM has been used to model natural and forced circulation molten salt loops[33]. However, the previous natural circulation models were larger, and thus did not have the low Reynolds number flow regimes in the present work. TRANSFORM was chosen as the modeling tool for this work because of its drag-and-drop setup, complex linear and non-linear solution routines, and emphasis on fundamental constitutive equations that allow for fast and accurate solutions with potential for easy reconfiguration. The generic default heat transfer and fluid flow models of TRANSFORM were used, i.e. no additional models specific to the problem were needed. The dimensions utilized in the model were taken from the drawing shown in Figure 1.

In the simulation, shown in Figure 11, each pipe was modeled as a single connected loop in TRANSFORM with multiple nodes within each pipe. The hot leg contained one node for each coupon, spacer and tensile bar, with a final empty node for the remaining empty section of pipe. A heat flux boundary condition of 1800 Watts (two 900 W heaters) was imposed on the pipe heat transfer surface. The sloped bottom leg, which was heated by another 900 W heater, was modeled with internal heat generation only, a simpler method. Generally, pipes that do not contain test samples such as the bottom leg can be modeled with less detail.

The cold leg pipes were modeled as pipes with a single heat transfer surface, as with the hot leg. The heat transfer surface is then given a convection resistance condition that is connected to an ambient temperature boundary condition of 21°C with the surface area determined by the geometry of the pipe. Typically, a boundary condition such as this will have a heat transfer coefficient (alpha [α]) determined by a Nusselt number correlation that relates the Raleigh number to the Nusselt number.

$$\alpha = \frac{Nu*k}{L} \quad \text{(T1)}$$

$$Nu = C_1 Ra^n \quad \text{(T2)}$$

$$Ra = GrPr \quad \text{(T3)}$$

$$Gr = \frac{g\beta\Delta T L^3}{\nu^2} \quad \text{(T4)}$$

$$Pr = \frac{C_p \mu}{k} \quad \text{(T5)}$$

Where:

L = Characteristic Dimension
k = Thermal conductivity
g = Gravitational constant
β = Coefficient of thermal Expansion ($1/T_{fluid}$)
$\Delta T = T_{surface} - T_{ambiant}$
ν = Kinematic viscosity
Cp= Specific heat capacity
μ = Dynamic viscosity

However, due to the presence of heat tape added to the piping components this correlation will not hold true and must be adjusted. To correct for the presence of a non-uniform heat tape, thermocouples were added to the model to match the positions at the inlet and outlet of each leg of the loop and monitored by a PID controller that was instructed to adjust the constants of the heat transfer coefficient to maintain the ΔT between the upper pipe and cold leg to match the measured ΔT. Resistances were added to the model to represent the various bends and pipe losses throughout the natural circulation loop and calibrated to give the proper delta T across the hot leg.

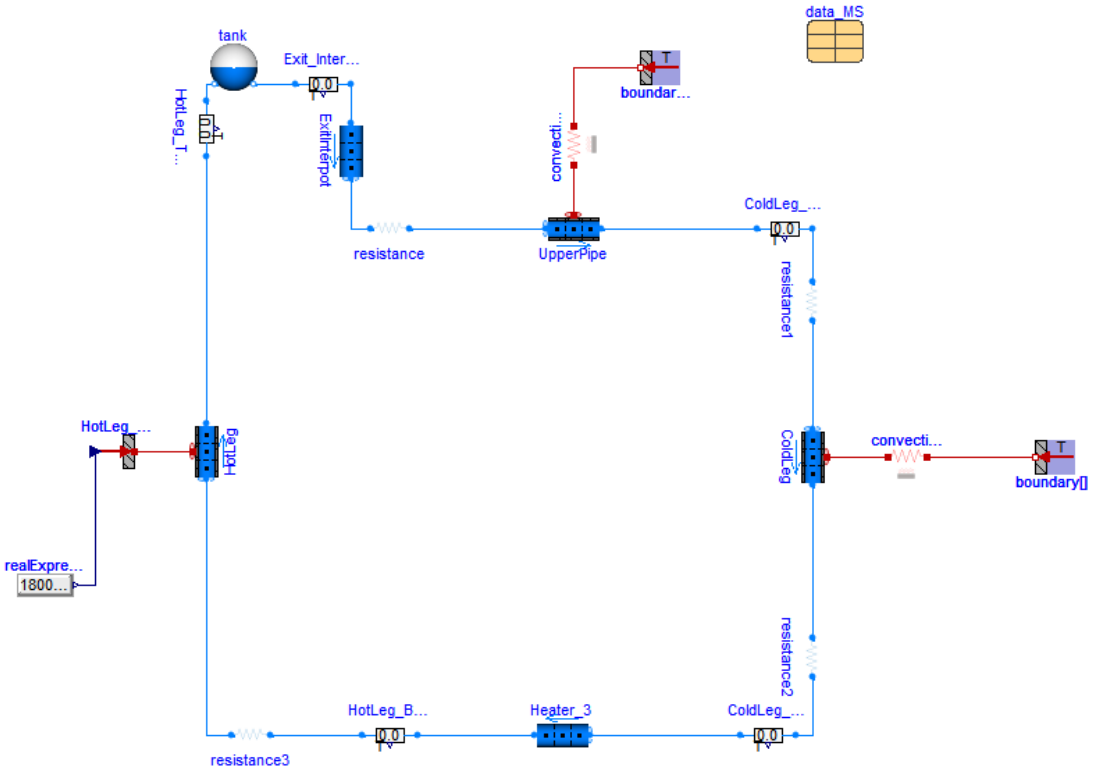

Figure 11. Schematic diagram of the TRANSFORM model of the TCL

The TRANSFORM model results were benchmarked against data taken on August 8th 2019 at 11:30 AM. At this point the loop had reached steady state operation at ~24 h of operation. The data points for the Bottom of the Hot Leg (BHL), Top of the Hot Leg (THL), Top of the Cold Leg (TCL), and Bottom of the Cold Leg (BCL) are shown in Figure 12, along with the results of the TRANSFORM simulation. The dotted black line at 24 h represents the steady state benchmark that was chosen for the simulation. Data are interspersed in their time scale. The first 10 datapoints were taken at approximately 5 to 10 minute intervals to ensure temperature was maintained at the beginning of the test, and later datapoints were taken 3-12 h apart once the loop was maintaining steady temperatures. Figure 12a shows the measured temperatures throughout the experiment with the results of the TRANSFORM simulation shown in Figure 12b.

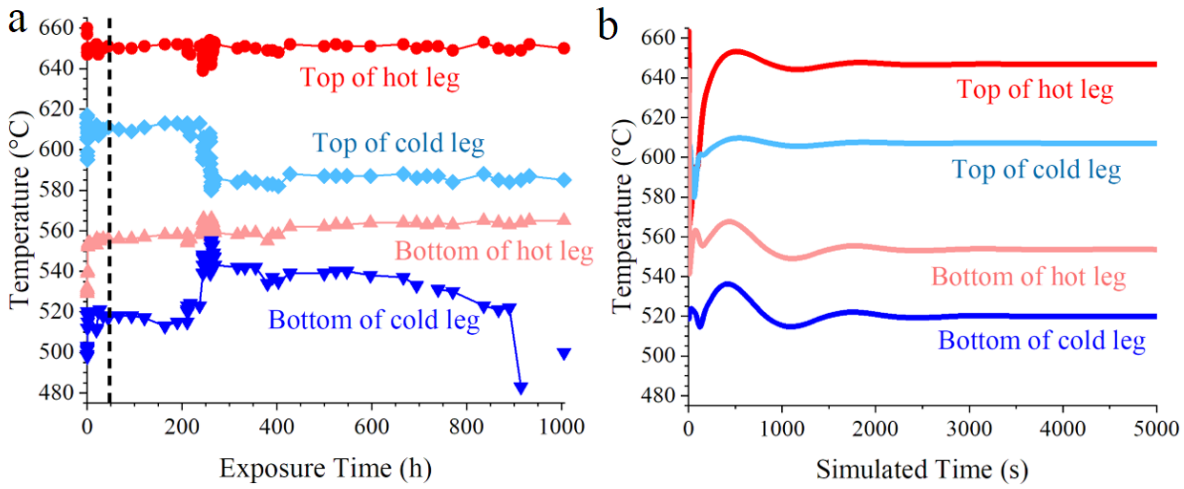

Figure 12. (a) measured temperature profile during the experiment and (b) TRANSFORM simulated temperatures at the thermocouple locations in the TCL. Simulations were based on the measured temperature at 24 h, indicated by the dotted line on (a).

The simulated thermocouples in the TRANSFORM model match those taken by the loop thermocouples. Temperatures once the simulation reached steady state are shown in Table 4.

Table 4. Comparison of Test Steady State (SS) and Simulation Steady State Temperatures

	Exit Interpot	ColdLeg TCL	Coldleg BCL	Hotleg BHL	HotLeg THL
Test SS Temperature (°C)	661	607	520	555	647
Simulated SS Temperature (°C)	661	607	520	554	647

With these general results in hand, the detailed simulation temperature distributions for the fluid surrounding the coupons will be representative of the fluid temperatures and flows during the test. Steady state mass flow values through the loop were determined to be 9.61×10^{-3} kg/s. The velocity profile around the coupons and spacers is shown for the hot and cold legs in Figure 13. Velocity was also measured during the experiment by locally heating an exposed section of the piping near the thermocouple at the bottom of the cold leg, and measuring the time for the temperature spike to reach the thermocouple at the bottom of the hot leg. This measurement yielded a velocity of 1.8 cm/s. Figure 14 shows the simulated temperature profile in the hot and cold legs. Position is indicated by the vertical distance from the bottom of the top pot.

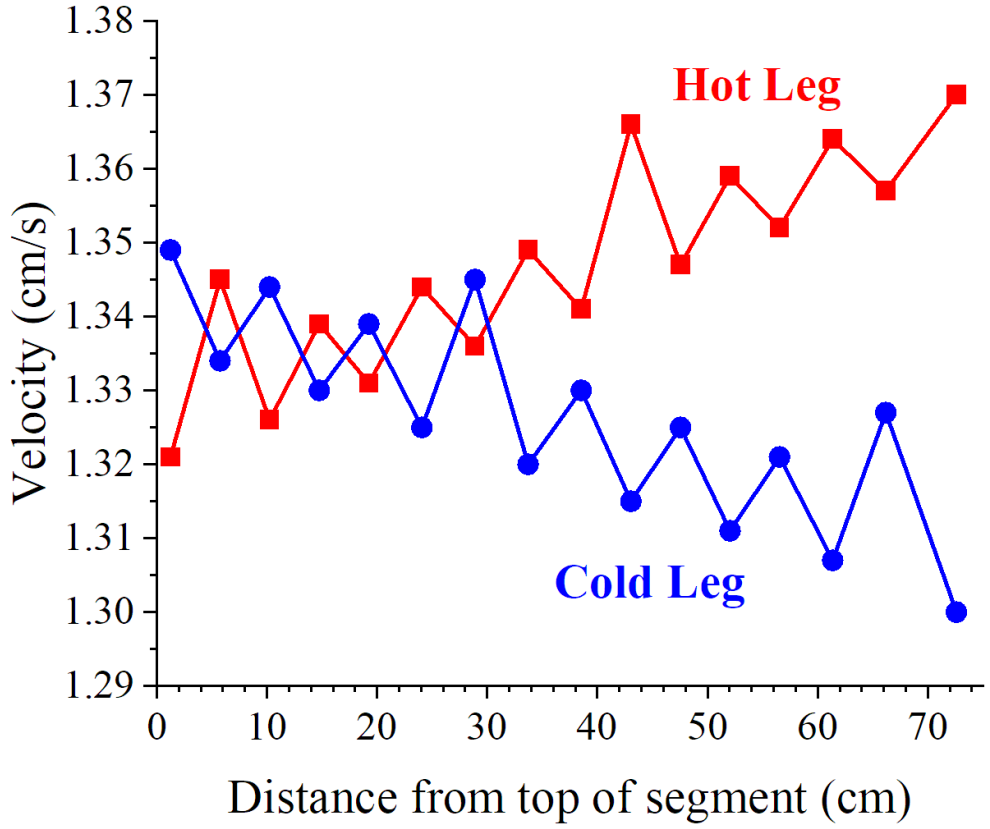

Figure 13. TRANSFORM modeled velocity profile in the hot leg and cold leg of the TCL.

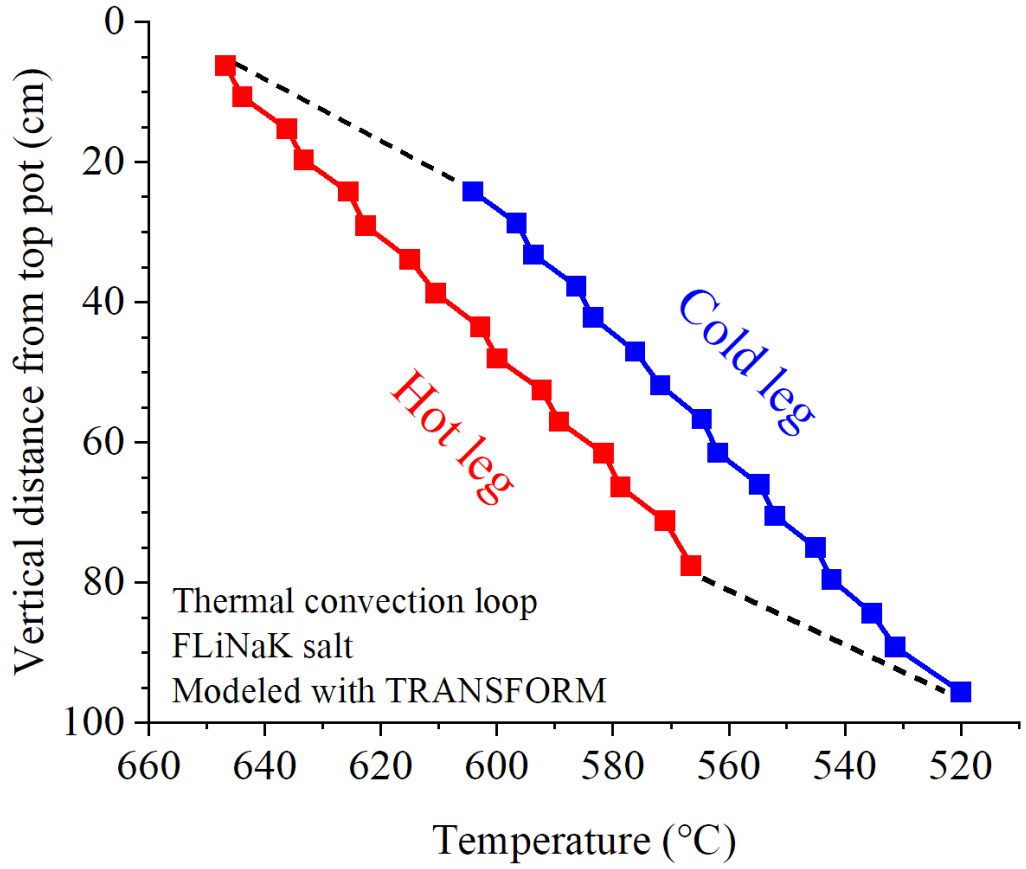

Figure 14. TRANSFORM modeled temperature profile in the hot and cold leg of the TCL.

Discusson

When analyzing the corrosion results, it is important to consider the ratio of the volume of salt to the surface area of wetted 316H surfaces. Figure 15 shows mass change divided by the ratio of salt volume to wetted surface area for the static and loop experiments. This figure accounts for all wetted 316H surfaces including the tubing and the capsule walls.

The volume to wetted surface area ratio in the loop is 0.9 $\frac{cm^3}{cm^2}$, and the ratio is 0.2 $\frac{cm^3}{cm^2}$ in the 316H capsules (the coupon area is 2.2 cm^2 and the wetted capsule area is 71.4 cm^2). The figure shows that the normalized mass loss of the hot leg sample was greater than the mass loss of the static experiments. This can be attributed to the mass transfer that occurred as salt flowed from the hot leg to the cold leg, and either leached or deposited corrosion product due to temperature-dependent reaction rate constants. The mass gain observed on the cold leg sample from the loop confirms this mass transfer. In the static capsule experiment at 550°C, a mass loss was observed, Figure 15.

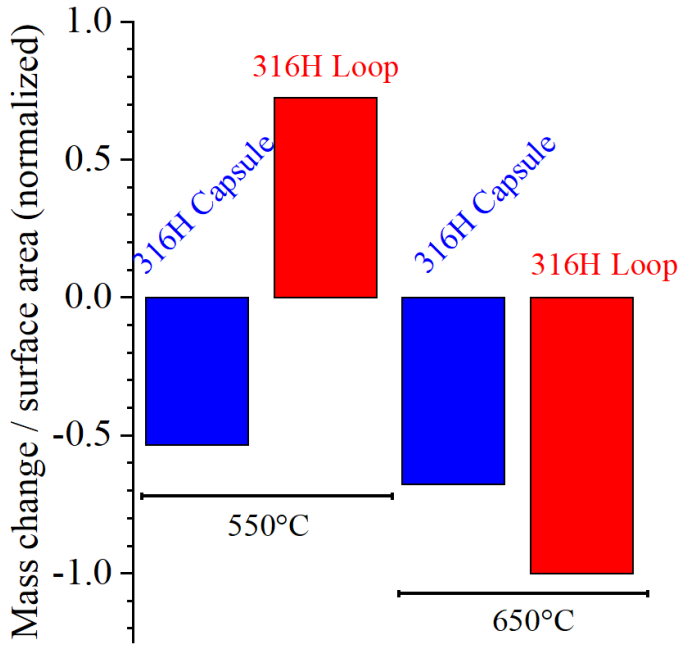

Figure 15. Normalized mass change of 316H samples exposed to FLiNaK salt for 1000 h in capsules or a TCL. Actual temperatures of the loop specimens were 552°C and 647°C.

Figure 8,Figure 9 show that the deposited layer on the cold leg samples was rich in Fe compared to the other alloy components. This may be surprising, since Figure 10 shows that Cr is the most abundant alloy constituent in the salt. This discrepancy can be explained in a few ways. First, it is possible that the Cr concentration in the salt never reached equilibrium in the hot leg, so the rate of deposition in the cold leg remained low. Dissolution of Cr into the salt would slow as the 316H surfaces became Cr depleted as shown in Figure 7. Another possibility is the kinetics of Fe deposition could be faster than the deposition kinetics of Cr. It is also possible that the solubility of Fe in the salt changes more strongly with temperature than the solubility of Cr. If ~250ppm Cr (Figure 10) is soluble in FLiNaK at 550°C, then there would be no driving force for deposition. However, the ~70 ppm Fe in the salt may reflect the solubility limit in the salt at 550°C and if higher Fe levels were present in the hot leg, mass transfer of Fe would be favored. Furthermore, since all of the surfaces are Fe-rich, the dissolution of Fe would continue throughout the experiment (unlike Cr which becomes depleted from all the specimens, Figure 7).

Figure 5 shows that all the samples in the cold leg, and the lower temperature samples in the hot leg, had a deposited layer on their surfaces. However, Figure 4 shows that only samples C10, C11, and C12 gained mass, indicating mixed mode corrosion in the other samples with a deposit. One possibility is that the samples lost their mass (e.g. Cr depletion in Figure 7) in the initial stages of exposure, while the salt corrosivity was presumably at its highest, and before the deposited layer formed on the sample surfaces. Another possibility is that Cr was still attacked after the formation of the deposited layer, but this is less likely because of the slow kinetics of Cr diffusion.

Conclusions

Demonstrating classic mass transfer behavior, type 316H samples in the hot leg of the FLiNaK thermal convection loop lost mass and samples in the cold leg gained mass. Samples in the intermediate range exhibited mixed mode corrosion with observed deposits, but overall mass loss. The hottest loop sample at 650°C lost more mass than a 316H sample exposed for the same time in the same FLiNaK salt but in a static capsule, exhibiting the accelerating effect of mass transfer. Examination of the cold leg samples from the loop showed that Fe was the primary deposited alloy constituent in the cold leg. The hot leg samples showed typical corrosion patterns, with Cr depletion near the surfaces. A TRANSFORM model of the loop matched the measured temperature profile, showing that it is a valid tool for modeling flowing molten salt in this experiment.

Acknowledgements

The authors acknowledge the assistance of Jim Keiser, Tracie Lowe, and Victoria Cox. This work was funded by the U.S. Department of Energy, Office of Nuclear Energy, Molten Salt Reactor Campaign.

References

[1] J. Serp, M. Allibert, O. Beneš, S. Delpech, O. Feynberg, V. Ghetta, D. Heuer, D. Holcomb, V. Ignatiev, J.L. Kloosterman, L. Luzzi, E. Merle-Lucotte, J. Uhlíř, R. Yoshioka, D. Zhimin, The molten salt reactor (MSR) in generation IV: Overview and perspectives, Progress in Nuclear Energy. 77 (2014) 308–319. https://doi.org/10.1016/j.pnucene.2014.02.014.

[2] D. LeBlanc, Molten salt reactors: A new beginning for an old idea, Nuclear Engineering and Design. 240 (2010) 1644–1656. https://doi.org/10.1016/j.nucengdes.2009.12.033.

[3] W.D. Manly, G.M. Adamson, J.H. Coobs, J.H. DeVan, D.A. Douglas, E.E. Hoffman, P. Patriarca, Aircraft reactor experiment-metallurgical aspects, ORNL-2349, (1957) 59.

[4] J.H. DeVan, R.B. Evans, Corrosion behavior of reactor materials in fluoride salt mixtures, ORNL-TM-0328, (1962) 1–39.

[5] J.W. Koger, A.P. Litman, ORNL-TM-2741 Catastrophic corrosion of type 304 stainless steel in a system circulating fused sodium fluoroborate, 1970.

[6] J.W. Koger, Evaluation of Hastelloy N Alloy After Nine Years Exposure to Both a Molten Fluoride Salt and At at Temperatures from 700 to 560C (ORNL/TM/4189), 1972.

[7] J.R. Keiser, Status of Tellurium - Hastelloy N Studies in Molten Fluoride Salts (ORNL TM-6002), 1977.

[8] J.R. Keiser, J.H. DeVan, E.J. Lawrence, Compatibility of molten salts with type 316 stainless steel and lithium, Journal of Nuclear Materials. 85–86, Par (1979) 295–298. https://doi.org/10.1016/0022-3115(79)90505-1.

[9] H. Ast, E.L. Lo, J.W. Koger, ORNL-TM-4188 EFFECT OF FeF, ADDITION ON MASS TRANSFER I N A THERMAL CONVECTION LOOP SYSTEM HELP HOME, (n.d.).

[10] B.-W.D. Manly, J.W. Allen, W.H. Cook, J.H. DeVan, D.A. Douglas, H. Inouye, D.H. Jansen, P. Patriarea, T.K. Roche, G.M. Slaughter, A. Taboada, G.A. Tolson, Construction Materials for Molten Salt Reactors, in: n.d.

[11] J.H. Devan, Effect of Alloying Additions of Corrosion Behavior of Nickel-Molybdenum Alloys in Fused Fluoride Mixtures (ORNL TM-2021), University of Tennessee, 1969.
[12] V. Ignatiev, A. Surenkov, 5 – Corrosion phenomena induced by molten salts in Generation IV nuclear reactors, in: Structural Materials for Generation IV Nuclear Reactors, 2017: pp. 153–189. https://doi.org/10.1016/B978-0-08-100906-2.00005-7.
[13] P.F. Tortorelli, J.H. Devan, J.R. Kaiser, CORROSION OF TYPE 316 STAINLESS STEEL IN MOLTEN LiF-LiCl-LIBr], Journal of Nuclear Materials. 103 (1981) 675–680.
[14] J.R. Distefano, J.H. Devan, J.R. Keiser, R.L. Klueh, W.P. Eatherly, Materials considerations for molten salt accelerator based plutonium conversion systems (ORNL/TM/12925/R1), (1995).
[15] J. Jun, K.A. Unocic, M.J. Lance, H.M. Meyer, B.A. Pint, Compatibility of FeCrAlMo with flowing PbLi at 500°-650 °C, Journal of Nuclear Materials. 528 (2020) 151847. https://doi.org/10.1016/j.jnucmat.2019.151847.
[16] V. Ignatiev, A. Surenkov, Alloys compatibility in molten salt fluorides: Kurchatov Institute related experience, Journal of Nuclear Materials. 441 (2013) 592–603. https://doi.org/10.1016/j.jnucmat.2013.05.007.
[17] K. Britsch, M. Anderson, P. Brooks, K. Sridharan, Natural circulation FLiBe loop overview, International Journal of Heat and Mass Transfer. 134 (2019) 970–983. https://doi.org/10.1016/j.ijheatmasstransfer.2018.12.180.
[18] B.A.B.A. Pint, J.W.J.W. McMurray, A.W.A.W. Willoughby, J.M.M. Kurley, S.R.S.R. Pearson, M.J.M.J. Lance, D.N. Leonard, H.M.H.M. Meyer, J. Jun, S.S.S.S. Raiman, R.T.R.T. Mayes, Re-establishing the paradigm for evaluating halide salt compatibility to study commercial chloride salts at 600°C–800°C, Materials and Corrosion. 70 (2019) 1439–1449. https://doi.org/10.1002/maco.201810638.
[19] B.A. Pint, S.S. Raiman, J.R. Keiser, Lifetime modeling for a supercritical CO<inf>2</inf>-molten salt CSP power block, in: AIP Conference Proceedings, 2019. https://doi.org/10.1063/1.5117668.
[20] H.E. McCoy, THE INOR-8 STORY., (1969).
[21] New Developments in Materials for Molten-Salt Reactors: Nuclear Applications and Technology: Vol 8, No 2, (n.d.). https://www.tandfonline.com/doi/abs/10.13182/NT70-A28622 (accessed June 4, 2021).
[22] R.H. Guymon, MSRE Systems and Components Performance (ORNL-TM-3039), 1973.
[23] G. Zheng, B. Kelleher, G. Cao, M. Anderson, T. Allen, K. Sridharan, Corrosion of 316 stainless steel in high temperature molten Li2BeF4 (FLiBe) salt, Journal of Nuclear Materials. 461 (2015) 143–150. https://doi.org/10.1016/j.jnucmat.2015.03.004.
[24] R.S. Sellers, W.-J. Cheng, B.C. Kelleher, M.H. Anderson, K. Sridharan, C.-J. Wang, T.R. Allen, CORROSION OF 316L STAINLESS STEEL ALLOY AND HASTELLOY-N SUPERALLOY IN MOLTEN EUTECTIC LiF-NaF-KF SALT AND INTERACTION WITH GRAPHITE, (n.d.). https://doi.org/10.13182/NT13-95.
[25] G. Zheng, L. He, D. Carpenter, K. Sridharan, Corrosion-induced microstructural developments in 316 stainless steel during exposure to molten Li2BeF4(FLiBe) salt, Journal of Nuclear Materials. 482 (2016) 147–155. https://doi.org/10.1016/j.jnucmat.2016.10.023.
[26] A. V. Abramov, I.B. Polovov, V.A. Volkovich, O.I. Rebrin, Corrosion of Austenitic Stainless Steels in Chloride Melts, Molten Salts Chemistry and Technology. (2014) 427–448. https://doi.org/10.1002/9781118448847.ch6e.

[27] J.R. Keiser, Compatibility studies of potential molten-salt breeder reactor materials in molten fluoride salts (ORNL/TM/5783), (1977).
[28] ASTM A53 / A53M - 20 Standard Specification for Pipe, Steel, Black and Hot-Dipped, Zinc-Coated, Welded and Seamless, (n.d.). https://www.astm.org/Standards/A53.htm (accessed September 17, 2020).
[29] D. Wilson, Personal Communication, 2017.
[30] L.C. Olson, J.W. Ambrosek, K. Sridharan, M.H. Anderson, T.R. Allen, Materials corrosion in molten LiF–NaF–KF salt, Journal of Fluorine Chemistry. 130 (2009) 67–73. https://doi.org/10.1016/j.jfluchem.2008.05.008.
[31] S.S. Raiman, R.T. Mayes, J.M. Kurley, R. Parrish, E. Vogli, Amorphous and partially-amorphous metal coatings for corrosion resistance in molten chloride salt, Solar Energy Materials and Solar Cells. 201 (2019) 110028. https://doi.org/10.1016/j.solmat.2019.110028.
[32] M.S. Greenwood, TRANSFORM - TRANsient Simulation Framework of Reconfigurable Models. Computer software, Oak Ridge National Laboratory., (2017). https://doi.org/10.11578/dc.20171025.2022.
[33] M.S. Greenwood, B.R. Betzler, A. Lou Qualls, J. Yoo, C. Rabiti, Demonstration of the Advanced Dynamic System Modeling Tool TRANSFORM in a Molten Salt Reactor Application via a Model of the Molten Salt Demonstration Reactor, Nuclear Technology. 206 (2020) 478–504. https://doi.org/10.1080/00295450.2019.1627124.